Far-field polarization characterization of the fundamental modes of a strip silicon waveguide

Jian Wang,* Justin C. Wirth, Yi Xuan, Daniel E. Leaird, Andrew M. Weiner, and Minghao Qi

School of Electrical and Computer Engineering and Birck Nanotechnology Center, Purdue University, 465 Northwestern Avenue, West Lafayette, Indiana 47906, USA

**Corresponding author: wang381@purdue.edu*

Received September 16, 2013; accepted October 2, 2013;
posted October 16, 2013 (Doc. ID 197719); published November 12, 2013

The fundamental quasi-TE and quasi-TM modes of a sub-wavelength strip silicon waveguide are not purely TE or TM as the plane waves in free space. We investigate theoretically and experimentally the far-field polarization compositions of the two waveguide modes after they emanate from the waveguide facet. The measured polarization extinction ratios (PERs) of 31 dB for the quasi-TM mode and 26 dB for quasi-TE mode using free-space polarizers are consistent with our numerical analysis. Moreover, our far-field simulations show that the free-space measurement of PERs is influenced, and in many cases limited, by the sizes of various apertures in the experimental setup. This suggests a potential trade-off between achievable PERs and overall power detection/collection efficiency.

OCIS codes: (230.3120) Integrated optics devices; (130.5440) Polarization-selective devices; (230.7370) Waveguides.
http://dx.doi.org/10.1364/OL.38.004785

Polarization diversity schemes [1,2] allow signals of unknown polarization states from input fibers to be processed by silicon photonic devices [3], which have strong structural birefringence. Meanwhile, for emerging modulation schemes such as polarization multiplexing [4], it is also desirable to launch a pure polarization with low cross talk into fibers from silicon photonic waveguides [5–7]. For such applications, it is necessary to understand what polarization extinction ratios (PERs) the fundamental modes of sub-wavelength silicon waveguides can achieve in free space, and this, to our best knowledge, has not been investigated quantitatively. Technically, one challenge was that for far-field simulations, the Gaussian beam decomposition method cannot be applied to obtain accurate numerical results due to the large beam divergence of waveguide modes [8]. Here we simulate the modes emanating from waveguide to free space by a finite-difference time-domain method (FDTD) and project the radiation fields to the far-field regime using a vector integral method.

Consider a strip silicon waveguide with a typical cross section of 500 nm × 250 nm (width × height) sitting on top of a SiO_2 substrate of infinite thickness. Here we choose the upper cladding to be air, since several recent polarization diversity schemes rely on air upper cladding [9,10]. The electric field energy compositions Ue_i ($i = x$, y, and z) of the fundamental quasi-TM mode (effective index $n_{\text{eff}} = 1.97$) at $\lambda_0 = 1.55$ μm are computed as 51.8%, 2.6%, and 45.6%, respectively (hereafter, we adopt the coordinate system defined in Fig. 1(a), where z is the propagation direction, and x is normal to the wafer plane). Ue_i is defined as the integral of energy density in the E_i component normalized to the integral of the sum of energy density in all electric components over one waveguide transverse cross section ($Ue_i = \iint \varepsilon |E_i|^2 \mathbf{ds}$). For the fundamental quasi-TE modes ($n_{\text{eff}} = 2.52$), the electric field energy compositions are computed as 0.4%, 76.3%, and 23.3%, respectively, (hereafter the two modes will be referred to as TM and TE modes). Compared to the TM mode, the TE mode behaves more similarly to a plane wave in bulk silicon, with a smaller longitudinal composition Ue_z.

When the modes propagate from the waveguide to air, they quickly diverge and evolve into spherical waves. Figure 1(a) shows simulated $|E_x|$ and $|E_z|$ field distribution of the TM mode at a vertical mid-plane of the waveguide by a FDTD solver MEEP [11]. Nontrivial backscattering into both SiO_2 substrate and air is observed,

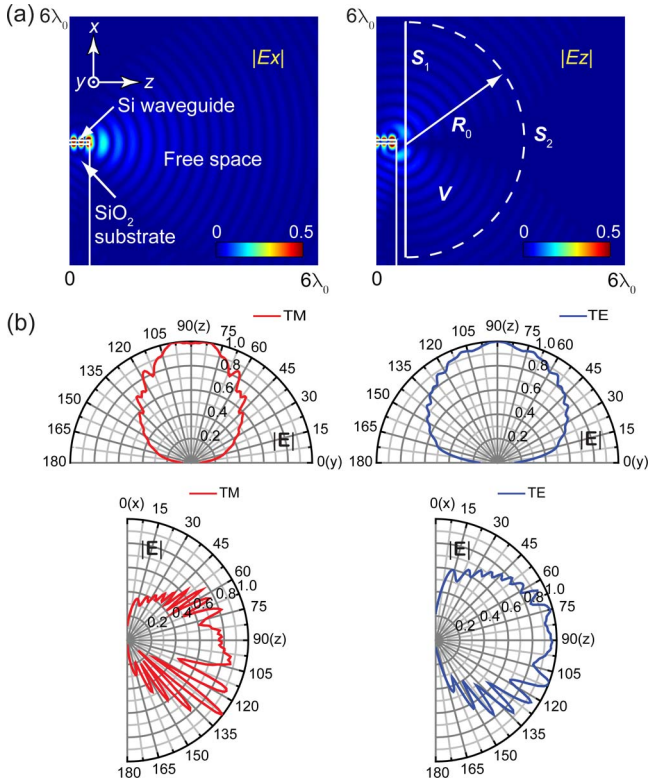

Fig. 1. (a) Near-field FDTD simulations of the fundamental TM mode emanating from a silicon waveguide to air. $|E_x|$ and $|E_z|$ are normalized to their respective maxima. (b) The radiation patterns of $|\mathbf{E}|$ of the TM and TE waveguide modes are plotted at the yz and xz planes.

which will be discussed later. The radiation patterns in Fig. 1(b) show wide beam divergences in both modes, which are very different from that of Gaussian beams [12]. Noticeably, the TE mode looks more isotropic in the far field than TM mode at both representative planes.

The radiation patterns of $|\mathbf{E}|$ can be obtained by projecting the electromagnetic fields close to the exit facet to the far-field regime. According to the vector Kirchhoff integral method,

$$\mathbf{E}(\mathbf{r}) = \oiint_S ds'\{i\omega(\mathbf{n}' \times \mathbf{B}(\mathbf{r}'))G + (\mathbf{n}' \times \mathbf{E}(\mathbf{r}')) \times \nabla' G + (\mathbf{n}' \cdot \mathbf{E}(\mathbf{r}'))\nabla' G\}, \quad (1)$$

$\mathbf{E}(\mathbf{r})$ at any point $\mathbf{r}$ within a volume V enclosed by a surface S can be represented by the fields $\mathbf{E}(\mathbf{r}')$ and $\mathbf{B}(\mathbf{r}')$ on S [here in Fig. 1(a), $S = S_1 + S_2$, S_2 is a semi-spherical surface of a radius R_0, and S_1 is a circular surface of the same radius]. $G(\mathbf{r}, \mathbf{r}') = \exp(ik|\mathbf{r} - \mathbf{r}'|)/(4\pi|\mathbf{r} - \mathbf{r}'|)$ is the 3D Green's function, and $\mathbf{n}'$ is directed into V. Since the integral over S_2 vanishes as R_0 goes to infinity, $\mathbf{E}(\mathbf{r})$ in the far field can be calculated based solely on the fields on S_1 close to the waveguide facet. Here, we choose S_1 as a square plane $30\lambda_0$ in size (the FDTD resolution is ~31 nm, or $\lambda_0/50$), which is $0.1\lambda_0$ away from the waveguide facet.

To understand the polarization characteristics of the two waveguide modes in the far-field regime, we first calculate the mode profiles at a plane 1 mm away from the waveguide exit facet based on Eq. (1). The square plane is 10 mm wide on each side, with a resolution of 10 μm. In Fig. 2, the far-field mode profiles feature the convolution of the near-field mode profiles and spherical waves for both modes: the major electric field component reaches its magnitude maximum around the center of the mode, whereas the minor components have nulls in the center and maxima away from the center.

Figure 2 shows that the measured PERs, defined as $\mathrm{PER_{TM}} = Ue_x/Ue_y$ and $\mathrm{PER_{TE}} = Ue_y/Ue_x$ for TM and TE modes, respectively, will be dependent on the sampling area. This is true in free-space characterization of polarization states, as only the light within a solid angle

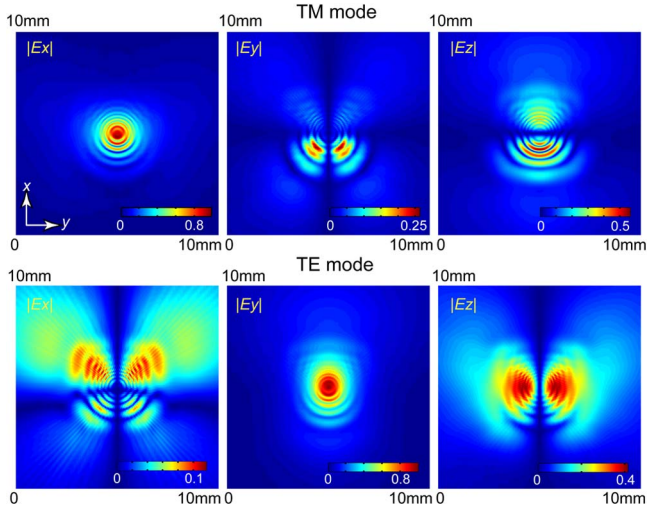

Fig. 2. Calculated far-field profiles of the TM and TE modes at a plane 1 mm away from the waveguide exit facet.

much smaller than 2π can be collected at the receiver. The magnitude of the angle is set by the sizes of various apertures in the measurement setup, such as that of objective, iris, polarizer, and photodetector. In light of this, we calculate and show in Fig. 3 how the values of Ue_i and PER are affected by the magnitude of the solid angle or the size of the aperture (denoted by the diameter d) at the fixed plane 1 mm away from the waveguide exit facet. For the TM mode, Ue_x decreases (Ue_y increases) with d as expected [Fig. 3(a)], and the $\mathrm{PER_{TM}}$ drops from ~60 to ~17dB when d increases from 0 to 2 mm [Fig. 3(c)]. The far-field energy compositions and $\mathrm{PER_{TE}}$ of the TE mode are also calculated and shown in Figs. 3(b) and 3(c), respectively. We find that the PERs of both modes are close in value at the same aperture diameter d.

To compare our analysis with experiments, we fabricated 500 nm × 250 nm (width × height) waveguides on an SOI wafer with a 3 μm thick SiO_2 buffer layer using the fabrication methods described in [13]. Characterization was accomplished with the experimental setup shown in Fig. 4(a), using fiber input and free-space coupling output, which has been the method used for the characterization of polarization rotators [1,14]. A 40× objective with a focal distance of 4.6 mm and a clear aperture of 8 mm was used to collect and collimate

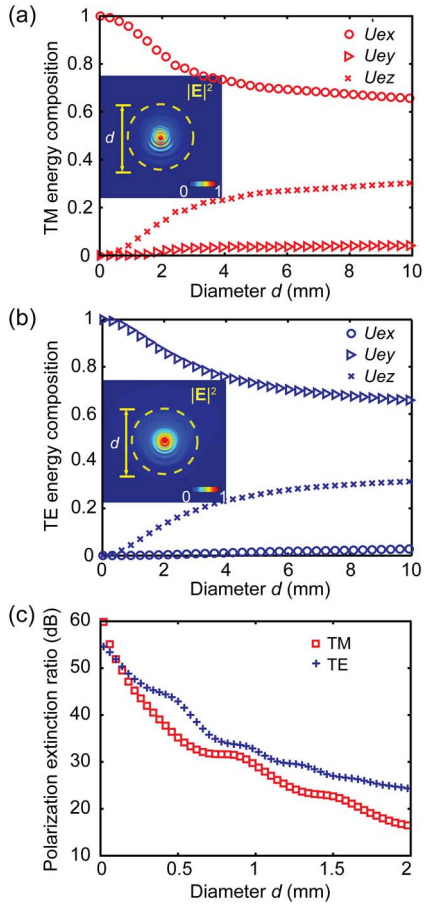

Fig. 3. Energy compositions, Ue_i, for (a) the TM mode and (b) TE mode at the 1 mm plane vary with the aperture diameter d. The insets are the profiles of the electric field energy densities $|\mathbf{E}|^2$. (c) The PERs of both TM and TE modes vary with the aperture diameter d.

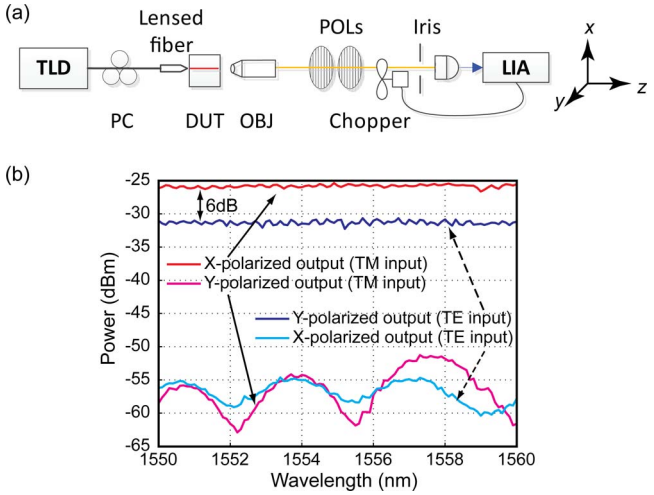

Fig. 4. (a) Experimental setup. TLD, tunable laser diode; PC, polarization controller; DUT, device under test; OBJ, objective; POLs, polarizers; LIA, locked-in amplifier. (b) Transmission spectra taken with both TE and TM linearly polarized CW inputs.

the output field. After a distance of 60 cm, light was then passed through a pair of rotatable polarizers, which combined to give a baseline PER of 43 dB. An adjustable iris was used to suppress detection of light coupled to the slab mode of the chip, with its aperture set at 5 mm. The photodetector used consists of a 5.8 mm diameter lens, which focuses onto a square sensor with an area of 1 mm × 1 mm. The input polarization was precisely set by removing the sample chip from setup and coupling the fiber tip directly to the objective. The polarization at the fiber tip was first set to TM with an extinction ratio of 40 dB at 1550 nm. The chip was then reinserted into the setup and aligned. Despite the 8 mm clear aperture in the objective lens, the 5 mm aperture of the iris reduces the aperture of the setup, which, along with the objective's focal distance of 4.6 mm, leads to an effective f–number around 1 for the setup, corresponding to $d = 1$ mm in Fig. 3(c).

Figure 4(b) shows the transmission spectra taken with both TM and TE polarized CW inputs. With the TM input, the $x(y)$ polarized output presents the major (minor) output component. With the TE input, the $y(x)$ polarized output presents the major (minor) output component. Based on the averaged transmission in Fig. 4(b), the experimental PER for TM input is $\mathrm{PER_{TM}} = P_x/P_y = 31$ dB and agrees well with the simulated value in Fig. 3(c) at $d = 1$ mm. On the other hand, for the TE input, the average experimental $\mathrm{PER_{TE}} = P_y/P_x = 26$ dB is lower than the simulated value of 32 dB.

To understand the discrepancy, we note that the linearly polarized light from the fiber input will excite in the strip waveguide both quasi-TE and quasi-TM modes, which have electric field components in the x and y directions. Another piece of evidence is that Fig. 1(b) shows the pure quasi-TE (or TM) mode to be significantly different from a plane-wave mode after exiting the waveguide, and, by reciprocity, a linearly polarized input cannot excite only one quasi-TE (or TM) mode.

To estimate the magnitude of the weak unwanted waveguide mode, we refer to Fig. 2(c) in [15] where an SOI microring resonator has a tunable input coupler that could be adjusted through the critical coupling condition. The best extinction ratio observed in transmission was 27 dB. In [10] when a polarization diversity scheme was applied to a similarly configured SOI microring, the extinction ratio approached 38 dB. These results suggest that the excited unwanted waveguide mode, which is off-resonance and responsible for the through-port transmission of the ring, may be upper bounded at the −27 dB level. Here we assume the excitation ratio of the unwanted waveguide mode to be at −30 dB.

Now we assume the linearly polarized TE input excites 0 dB quasi-TE mode and −30 dB quasi-TM mode. Figure 4(b) shows that the quasi-TE mode suffers 6 dB higher transmission loss than the quasi-TM mode. Therefore at the output, the quasi-TM mode will only be 24 dB lower than the quasi-TE mode. The detected x polarization in free space, consisting of the sum of the major component of the unwanted quasi-TM mode and the minor component of the quasi-TE mode, will be ∼24 dB lower than the y polarization, regardless of how high the PER of the quasi-TE mode is. This estimated $\mathrm{PER} = P_y/P_x$ of 24 dB is now consistent with the experimental value of $\mathrm{PER_{TE}}$ of 26 dB. A similar analysis for the linearly polarized TM input, on the other hand, shows that $\mathrm{PER_{TM}}$ will not suffer such a limitation.

Finally, the 6 dB transmission difference between the major component outputs of the TM (red) and TE (blue) inputs in Fig. 4(b) can be accounted for by the mode-dependent facet transmission/reflection and waveguide propagation loss. The facet transmission coefficient t and reflection coefficient r can be calculated using FDTD, the values of which are listed in Table 1. Significant backscattering, characterized by a coefficient $s = 1 - r - t$, was also observed in the FDTD simulations [also shown in Fig. 1(a)]. The waveguide propagation loss was retrieved from experimental data based on a Fabry–Perot (FP) cavity model [16]. In general, the power transmission through a FP cavity is given by

$$T = \eta \frac{t^2 e^{-2\alpha L}}{(1 - re^{-2\alpha L})^2 + 4re^{-2\alpha L}\sin^2(\theta/2)}, \tag{2}$$

where L is the guide length, $\gamma = \exp(-2\alpha L)$ is the round-trip field attenuation factor, s, r, and t coefficients refer to power, and θ denotes the round-trip phase shift. The coupling efficiency from a fiber mode to a waveguide mode, η, is assumed the same for both polarizations.

Table 1. Parameters Used in the FP Model

Polarization	Item	Symbol	Value
TM	Facet transmission coe.	t	64%
	Facet reflection coe.	r	16%
	Facet scattering coe.	s	20%
	FP transmission depth	$T_{\max}/T_{\min}$	0.5 dB
	Field attenuation factor	$e^{-2\alpha L}$	0.18
TE	Facet transmission coe.	t	38%
	Facet reflection coe.	r	33%
	Facet scattering coe.	s	29%
	FP transmission depth	$T_{\max}/T_{\min}$	0.75 dB
	Field attenuation factor	$e^{-2\alpha L}$	0.13

Letting T_{max} and T_{min} denote the maximum and minimum of Eq. (2), γ can be expressed as

$$\gamma = \frac{1}{r}\frac{\sqrt{T_{max}/T_{min}} - 1}{\sqrt{T_{max}/T_{min}} + 1}. \quad (3)$$

With the measured transmission depths T_{max}/T_{min} of 0.5 dB for the quasi-TM mode and 0.75 dB for the quasi-TE mode in Fig. 4(b), we estimated $\gamma_{TM} = 0.18$ and $\gamma_{TE} = 0.13$. We thus calculated the averaged waveguide transmissions for the two modes as $T_{TM} = 0.074\eta$ and $T_{TE} = 0.019\eta$, respectively. This corresponds to a transmission ratio of 5.9 dB, which is consistent with our experimental observation.

Our analysis so far is for a particular cross section of 500 nm × 250 nm, but we expect similar effects exist for other similar cross sections.

Our finding has potential practical implications. In polarization diversity modulation schemes, low coupling loss is important. However, our results show that, at least for the free-space butt coupling, there is a trade-off between the d, or collection aperture, and the PER: a larger aperture will allow higher power collection efficiency but with a reduced PER. It is possible that various inverse taper structures or spot converters [17] could be adopted to convert the strip waveguide modes close to the fiber modes, and this will be further investigated.

In summary, the far-field mode profiles of the strip waveguide feature the convolution of the near-field mode profiles and spherical waves, which display different polarization characteristics from linearly polarized light in free space. The measurable PERs of the waveguide modes are influenced by the sizes of various apertures in the experimental setup. The values also can be affected at the presence of an unwanted waveguide mode excited by the fiber input. The finding here suggests a possible trade-off in the PER measurement of integrated polarization rotators using free-space polarizers, where care must be taken to the choice of aperture sizes and detectable power level.

The authors thank Professor Peter Bermel for his discussion. This work is supported by the National Science Foundation grants ECCS-0925759, ECCS-0901383, and CMMI-1120577; the Air Force Office of Scientific Research grant FA9550-08-1-0379, the National Institute of Health grant 1R01RR026273-01, and the Defense Advanced Research Projects Agency grant N66001-08-1-2037.

References

1. M. R. Watts, M. Qi, T. Barwicz, L. Socci, P. T. Rakich, E. I. Ippen, H. I. Smith, and H. A. Haus, in *Optical Fiber Communication Conference* (Optical Society of America, 2005), paper PDP11.
2. T. Barwicz, M. R. Watts, M. A. Popovic, P. T. Rakich, L. Socci, F. X. Kartner, E. P. Ippen, and H. I. Smith, Nat. Photonics **1**, 57 (2007).
3. H. Fukuda, K. Yamada, T. Tsuchizawa, T. Watanabe, H. Shinojima, and S. Itabashi, Opt. Express **16**, 2628 (2008).
4. K. Kikuchi, Opt. Express **19**, 17985 (2011).
5. L. Chen, C. R. Doerr, and Y. Chen, Opt. Lett. **36**, 469 (2011).
6. P. Dong, C. Xie, L. Chen, L. L. Buhl, and Y. Chen, in *European Conference and Exhibition on Optical Communication* (Optical Society of America, 2012), paper Th3B1.
7. J. Zhang, M. Yu, G. Lo, and D. Kwong, IEEE J. Sel. Top. Quantum Electron. **16**, 53 (2010).
8. N. Mortensen and J. Folkenberg, Opt. Express **10**, 475 (2002).
9. D. Dai and J. E. Bowers, Opt. Express **19**, 10940 (2011).
10. Y. Ding, B. Huang, H. Ou, F. Da Ros, and C. Peucheret, Opt. Express **21**, 7828 (2013).
11. A. F. Oskooi, D. Roundy, M. Ibanescu, P. Bermel, J. D. Joannopoulos, and S. G. Johnson, Comput. Phys. Commun. **181**, 687 (2010).
12. J. Wang, J. Ouyang, L. T. Varghese, L. Fan, Y. Xuan, and M. Qi, Adv. Opt. Mater. **1**, 740 (2013).
13. L. Fan, J. Wang, L. T. Varghese, H. Shen, B. Niu, Y. Xuan, A. M. Weiner, and M. Qi, Science **335**, 447 (2012).
14. J. C. Wirth, J. Wang, B. Niu, Y. Xuan, L. Fan, L. T. Varghese, D. E. Leaird, and A. Weiner, in *Conference on Lasers and Electro-Optics* (Optical Society of America, 2012), paper JW4A.83.
15. M. H. Khan, H. Shen, Y. Xuan, L. Zhao, S. Xiao, D. E. Leaird, A. M. Weiner, and M. Qi, Nat. Photonics **4**, 117 (2010).
16. T. Feuchter and C. Thirstrup, IEEE Photon. Technol. Lett. **6**, 1244 (1994).
17. V. R. Almeida, R. R. Panepucci, and M. Lipson, Opt. Lett. **28**, 1302 (2003).